Scattering of GPS Signals from the Ocean with Wind Remote Sensing Application

Valery U. Zavorotny and Alexander G. Voronovich

***Abstract*—A theoretical model that describes the power of a scattered Global Positioning System (GPS) signal as a function of geometrical and environmental parameters has been developed. This model is based on a bistatic radar equation derived using the geometric optics limit of the Kirchhoff approximation. The waveform (i.e., the time-delayed power obtained in the delay-mapping technique) depends on a wave-slope probability density function, which in turn depends on wind. Waveforms obtained for aircraft altitudes and velocities indicate that altitudes within the interval 5–15 km are the best for inferring wind speed. In some regimes, an analytical solution for the bistatic radar equation is possible. This solution allows converting trailing edges of waveforms into a set of straight lines, which could be convenient for wind retrieval. A transition to satellite altitudes, together with satellite velocities, makes the peak power reduction and the Doppler spreading effect a significant problem for wind retrieval based on the delay-mapping technique. At the same time, different time delays and different Doppler shifts of the scattered GPS signal could form relatively small spatial cells on sea surface, suggesting mapping of the wave-slope probability distribution in a synthetic-aperture-radar (SAR) fashion. This may allow more accurate measurements of wind velocity and wind direction.**

***Index Terms*—Bistatic rough surface scattering, sea surface remote sensing.**

I. Introduction

SIGNALS of the Global Positioning System (GPS) can be used for purposes other than navigation and positioning. Direct GPS signals are already being used to obtain low-cost atmospheric profiles by spaceborne receivers. Martin-Neira [1] first suggested using scattered signals from the existing net of 24 GPS satellites for ocean altimetry. Anderson [2] proposed to use the GPS signal interference pattern for a tide height determination in coastal regions. The experimental evidence that scattering of the GPS signal from the ocean surface can be detected onboard an airplane [3] generated more enthusiasm. Katzberg and Garrison [4] proposed to pick up the scattered GPS signal with a receiver onboard a low-orbiting satellite to determine ionospheric delay over the ocean. Pioneering experiments [5] recently have been carried out in which scattering of the GPS signal from the ocean surface has been detected by an airborne, delay-mapping GPS receiver. Plans are being considered to launch satellites with GPS receivers onboard to track GPS signals reflected from the ocean surface in order to investigate the possibility of ocean altimetry and scatterometry. These suggestions need to be substantiated by more careful theoretical modeling of the performance of such a receiver. Without this modeling, it would be difficult to successfully implement any of the foregoing technical ideas. Qualitative estimation of the performance of the delay-mapping receiver has been presented in [6]. The combination of GPS transmitters and a GPS delay-mapping receiver with a downlooking antenna can be also regarded as a multistatic radar-scatterometer. The peculiarity of such a GPS multistatic scatterometer is that the forwardscatter character of this technique can provide information about the ocean surface complementary to that obtained with conventional backscatter scatterometers. The theoretical assessment of the possibility of measuring wind speed using this technique was investigated in [7]. A comparison between this theoretical model and GPS reflected signal measurements taken from aircraft has been made to explore the possibility of determining wind speed [8], [9]. The inferred wind speed, obtained by comparing actual and modeled signals, shows good agreement with *in situ* measurements. Here, we present a thorough and extended analysis of this theoretical model.

Manuscript received February 16, 1999; revised October 22, 1999. This work was supported by E. Lindstrom of NASA Headquarters under the Physical Oceanography Program RTOP 622-47-55.

The authors are with the Cooperative Institute for Research in Environmental Sciences, Environmental Technology Laboratory, University of Colorado/NOAA, Boulder, CO 80303 USA.

Publisher Item Identifier S 0196-2892(00)02834-5.

II. Description of the Emitted GPS Signal

The temporal structure of the GPS direct signal is quite complicated. The GPS signal consists of two highly stable, almost monochromatic carriers, L1 and L2, upon which three modulations are impressed: the C/A code, the P-code, and the broadcast message [10]–[12]. All components of the GPS signal are based upon the fundamental clock rate $f_0 = 10.23$ MHz. The GPS carriers are at $f_1 = 154 f_0$ (L1) and $f_2 = 120 f_0$ (L2). The method of modulating the carrier is a binary biphase modulation. The two codes are periodic pseudo-random noise (PRN) codes. This type of modulation has been known in communication and radar techniques for quite a long time (cf., [13], [14]). The P-code is at the code modulation frequency $f_{m,P} = f_0$, and the C/A code is at $f_{m,C/A} = f_0/10$. According to these frequencies, a biphase modulation function $a(t)$ acquires values either $+1$ (normal state) or -1 (mirror image state). These states of the modulation function are called "chips" rather than bits, to indicate that they do not carry data. One chip lasts a period of time $\tau_c = 1/f_m$ and has a length $r_c = c\tau_c$. The carrier is modulated when it is multiplied by $a(t)$. Each transition of $a(t)$ from $+1$ to -1 or from -1 to $+1$ leads to a 180° phase shift of the carrier. The code sequence periodically repeats itself. For example, the C/A code has a length of 1023 chips, or a period of 1 ms. This phase modulation spreads the signal over a wide bandwidth, and it is usually referred to as a spread-spectrum technique. As a result of this spectral spreading, the signal cannot be

detected without knowledge of the coding function $a(t)$. Only a "despreading" processing procedure using cross-correlation between the signal and the coding function allows the signal to be restored.

Even though the phase modulation produced significant widening of the GPS signal, it remains a narrowband or quasi-monochromatic type, because $f_m \ll f_{1,2}$. Therefore, the direct GPS signal can be considered a quasimonochromatic, phase-modulated, spherical wave. The complex amplitude U of this signal at the receiver position $\vec{R}_r$ can be written as follows:

$$U(\vec{R}_r,t)=\frac{1}{R_d}a(t-R_d/c)\exp(iKR_d-2\pi i f_{1,2}t) \quad (1)$$

where $R_d \equiv |\vec{R}_d| = |\vec{R}_r - \vec{R}_t|$ is the distance from a transmitter at $\vec{R}_t$ to the receiver at $\vec{R}_r$; $K = K(f_{1,2}) = 2\pi f_{1,2}/c$. In principle, the function $a(t)$ could describe not only the phase modulation but any kind of modulation (amplitude, frequency, pulse, etc.). Note that the modulation signal $a(t-R_d/c)$ as well as the carrier wave, propagates at the speed of light c. In general, both the receiver and the transmitter are moving, therefore, R_d is a function of time. For the short time interval needed to process the signal, this dependence can be neglected everywhere except for the phase factor in (1). The relative motions of the transmitter and the receiver produce a Doppler shift in the received signal. It can be obtained by expanding $R_d(t=t_0+t')$ near t_0

$$\begin{aligned}|\vec{R}_d(t_0+t')| &\approx |\vec{R}_r(t_0)-\vec{R}_t(t_0)+t'[\vec{V}_r(t_0)-\vec{V}_t(t_0)]|\\ &\approx R_d(t_0)+t'[\vec{V}_r(t_0)-\vec{V}(t_0)]\cdot\nabla R_d(t_0) \quad (2)\end{aligned}$$

where $\vec{V}_t$ and $\vec{V}_r$ are velocity vectors of the transmitter and the receiver, respectively. Therefore, for the case of a moving transmitter and receiver, (1) becomes

$$U(\vec{R}_r,t)=U(\vec{R}_r,t_0)\exp[-2i\pi(f_{1,2}+f_D)t'] \quad (3)$$

where $f_D(t_0) = [\vec{V}_t(t_0) - \vec{V}_r(t_0)]\cdot\vec{\kappa}(t_0)/\lambda$ is the Doppler shift, and $\vec{\kappa}(t_0) = \nabla R_d(t_0)$ is the unit vector pointing from a transmitter to a receiver. Usually, this Doppler shift caused by relative motions of the transmitter and receiver is monitored by the conventional GPS receiver and it can be compensated for, along with other Doppler shifts caused by ionospheric and tropospheric irregularities.

III. Theoretical Model for Scattering of GPS Signal from the Ocean Surface

A. Description in Terms of Instantaneous Fields

Because of the relatively low power and remoteness of GPS transmitters, one can expect to receive the scattered signal only from the area around a nominal specular point on the mean sea surface, a so-called glistening zone [4]–[6]. The quasi-specular reflections generally dominate in this situation. According to the two-scale (or composite) roughness model [15], [16], this type of scattering is produced mostly by a large-scale (larger than several radio wavelengths) component of the surface. A power scattered toward the receiver decreases significantly on the periphery of the glistening zone until reaching the level where Bragg resonant scattering from a small-scale surface component starts to play a role. However, that type of scattering is not considered here because it is too weak to be detected by the current receivers. That allows us to account here only for the field scattered by the large-scale surface component and to use the Kirchhoff approximation for this purpose. We are not going to discuss limits of applicability of this approximation. This issue has been investigated intensively in numerous papers and books (cf., [16]–[19]). Examples of models similar to ours and based on the Kirchhoff approximation are also numerous (cf., [15], [20]–[22]). Hence, the scattered field in the Kirchhoff approximation is

$$u(\vec{R}_r,t)=\frac{1}{4\pi}\int D(\vec{R}_s,t)\Re\frac{\partial}{\partial N}\left[U(\vec{R}_s)\frac{\exp(iKR)}{R}\right]. \quad (4)$$

Here, $D(\vec{R}_s)$ is the footprint function of the receiving antenna in terms of complex amplitudes, $\Re$ is the polarization sensitive reflection coefficient, $\partial/\partial N$ is a normal derivative, $U(\vec{R}_s,t)$ is an incident field taken at $\vec{R}_s$ on the large-scale rough surface Σ, and $R(t) = |\vec{R}_r - \vec{R}_s|$ is the distance from the receiver to the point $\vec{R}_s$. When considering geometrical parameters such as the transmitter and receiver altitudes, signal time delays, etc., we always regard the Earth's surface as spherical. For satellite-borne receivers, the Earth's curvature produces some effect on a strength of surface scattering. However, estimations show that for airplane or balloon altitudes (about or less than several tens of kilometers), this effect is negligible, and a spherical surface can be replaced with a plane one. It is convenient to center our Cartesian coordinate system at the nominal specular point on a spherical ocean surface with the xy plane tangent to this surface, z-axis directed upward, and the yz plane an incidence plane. For a given transmitter altitude H_0 and receiver altitude H with respect to the spherical Earth's surface and angular distance α between them, one can find corresponding altitudes h_0 and h with respect to the xy plane (see Fig. 1).

Therefore, we assume that rough surface Σ within some limited area can be represented as a single-valued function $\zeta(\vec{r},\mathbf{t})$ of the plane vector $\vec{r} = (x,y,0)$ with $\langle\zeta\rangle = 0$. Then, we transform the integration over the surface Σ to the integration over vector $\vec{r}$. Derivative $\partial/\partial N$ in (4) is calculated using (1) for the incident field $U(\vec{R}_s)$ at $\vec{R}_s \equiv \vec{R}_s(\vec{r},\zeta(\vec{r},t))$. After neglecting derivatives of slow-changing functions a, $(R_0R)^{-1}$ and taking derivatives of a remainder, we obtain the following expression for the scattered field:

$$u(\vec{R}_r,t)=\int D(\vec{r})a[t-(R_0-R)/c]g(\vec{r},t)\,d\vec{r} \quad (5)$$

where $R_0(t) = |\vec{R}_s - \vec{R}_t|$ is the distance from the transmitter at $\vec{R}_t$ to the point $\vec{R}_s$ on the rough surface, and

$$g(\vec{r},t)=-\Re\frac{\exp(-2\pi i f_{1,2}t)}{4\pi i R_0R}\exp[iK(R_0+R)]\frac{q^2}{q_z}. \quad (6)$$

In (6), q_z stands for the z-component of the scattering vector $\vec{q} \equiv (q_z,\vec{q}_\perp)$

$$\begin{aligned}\vec{q} &= -K(\nabla_r R+\nabla_r R_0)\equiv K(\vec{R}/R-\vec{R}_0/R_0)\\ &\equiv K(\vec{n}-\vec{m}). \quad (7)\end{aligned}$$

Hence, $\vec{m}$ is the unit vector of the incident wave, and $\vec{n}$ is the unit vector of the scattered wave. For the case of $\zeta(\vec{r},t) \equiv 0$

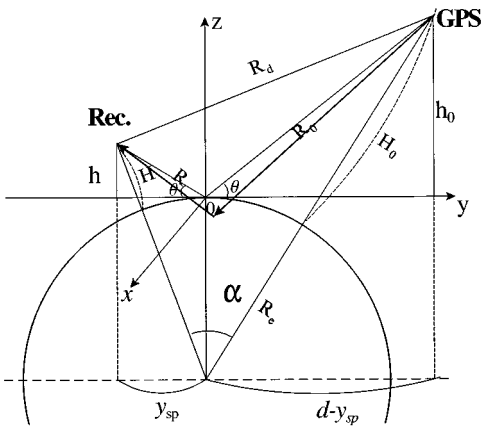

Fig. 1. Geometry of the problem.

(i.e., for an absolutely even, mirror-like spherical surface) the answer can be readily obtained by replacing an actual source with a mirrored one below the surface. Then, the reflected field is proportional to the field of a point source at distance $R_{0,\mathrm{sp}} + R_{\mathrm{sp}}$

$$u(\vec{R}_r, t) \sim \Re \frac{\exp[iK(R_{0,\mathrm{sp}} + R_{\mathrm{sp}})]}{(R_{0,\mathrm{sp}} + R_{\mathrm{sp}})} D(0) \cdot a\left[t - \frac{R_{0,\mathrm{sp}} + R_{\mathrm{sp}}}{c}\right], \quad (8)$$

where $R_{0,\mathrm{sp}} = |\vec{R}_t|$ and $R_{\mathrm{sp}} = |\vec{R}_r|$, because the specular point lies in the center of the coordinate system. This result can be obtained more rigorously from (5) and (6) using the stationary phase method (see, e.g., [16]) Therefore, the received signal has the same modulation function a with an argument shifted by the fixed value $(R_{0,\mathrm{sp}} + R_{\mathrm{sp}})/c$. Note that the coordinates of the transmitter and receiver are determined, respectively, by the vectors

$$\vec{R}_t = (0, d - y_{\mathrm{sp}}, h_0), \quad \vec{R}_r = (0, -y_{\mathrm{sp}}, h), \quad (9)$$

where parameters $d = (h_0 + h)/\tan\theta$ and $y_{\mathrm{sp}} = hd/(h_0 + h)$ are explained in Fig. 1. The elevation angle θ with respect to the nominal specular point is shown in Fig. 1 and defined here as an angle between vector of transmitter, $\vec{R}_t$ (or receiver, $\vec{R}_r$), and the horizontal plane. Correspondingly, vectors $\vec{R}_0$ and $\vec{R}$ from (6) and (7) can be expressed as

$$\vec{R}_0 = (x, y + y_{\mathrm{sp}} - d, -h_0), \quad \vec{R} = (-x, -y - y_{\mathrm{sp}}, h). \quad (10)$$

Analogously, the scattering vector $\vec{q}$ from (7) can also be expressed in terms of h, h_0, and θ.

Now consider all possible causes for a Doppler shift of a scattered signal. Since reflection from various surface areas is involved in the formation of the resultant wave phase, the position and the velocity of a reflecting patch plays an important role in a resultant Doppler shift. For time-dependent values in the exponent of (6), we can use expansions analogous to (2), assuming that the time interval t' is relatively small

$$R_0(t_0 + t') = |\vec{R}_s - \vec{R}_t| \approx R_0(t_0) + t'[\vec{v}_s - \vec{V}_t] \cdot \vec{m}(t_0),$$
$$R(t_0 + t') = |\vec{R}_r - \vec{R}_s| \approx R(t_0) + t'[\vec{V}_r - \vec{v}_s] \cdot \vec{n}(t_0) \quad (11)$$

where $\vec{V}_t$, $\vec{V}_r$, and $\vec{v}$ are velocity vectors of the transmitter, receiver, and the rough surface, respectively. Therefore, (6) becomes

$$g(\vec{r}, t_0 + t') = g(\vec{r}, t_0) \exp\{-2\pi i[f_{1,2} + f_D(\vec{r}, t_0)]t'\} \quad (12)$$

where

$$f_D = f_{D,0} + f_s \quad (13)$$

is a total Doppler shift, and

$$f_{D,0}(\vec{r}, t_0) = [\vec{V}_t \cdot \vec{m}(\vec{r}, t_0) - \vec{V}_r \cdot \vec{n}(\vec{r}, t_0)]/\lambda,$$
$$f_s(\vec{r}, t_0) = \vec{q}(\vec{r}, t_0) \cdot \vec{v}(\vec{r}, t_0)/2\pi. \quad (14)$$

The component $f_{D,0}$ describes the contribution to the Doppler shift due to the transmitter and receiver motions and due to various possible positions of the vector $\vec{r}$ in the surface mean plane $z = 0$, and f_s is caused by intrinsic motions of the surface. The surface velocity $\vec{v}(\vec{r})$ can be further split into various components due to currents, surface waves, etc. However, for an ocean surface $q_\perp \ll q_z$, therefore, the contribution to f_s is given mostly by the vertical component v_z of the orbital velocity of surface gravity waves

$$f_s \approx q_z v_z/2\pi. \quad (15)$$

Even assuming that $f_{D,0}$ can be compensated within some spatial zone by technical means, fluctuating f_s can still affect the signal.

B. Derivation of the Range-Coded Doppler-Limited Footprint Function

In the GPS receiver, the signal u obtained from the antenna output at a time $t_0 + \tau$ is cross-correlated with a replica of PRN code a taken at a different time t_0 (cf., [12])

$$Y(t_0, \tau) = \int_0^{T_i} a(t_0 + t')u(t_0 + t' + \tau)\exp(2\pi i f_c t')\, dt' \quad (16)$$

where T_i is the integration time. It is much larger than the chip duration τ_c and should be smaller than the length of one period of the code sequence $a(t)$ to avoid an ambiguity problem. For the successful demodulation of a signal, T_i also should be smaller than the correlation time related to the possible random variations of the signal $u(t)$ acquired during propagation or scattering processes. The oscillating factor containing f_c is aimed to compensate a possible Doppler shift of the signal $u(t)$. In the case of a direct signal, $u(t)$ is simply proportional to $a(t)$ taken with some time offset t_{off} caused by propagation from the transmitter to the receiver. The procedure in (16) is used to "despread" the signal. This is achieved by cross-correlating the received signal with the code replica for various time delays τ. The maximum correlation indicates that at the time delay $\tau = t_{\mathrm{off}}$, the two codes are aligned. Once the maximum is reached the code modulation is removed, and the signal becomes "despread." The time offset t_{off} extracted from the direct signal provides information about the range between the GPS transmitter and the GPS receiver, which is used for navigational purposes. For the case of the GPS signal scattered from Earth's

surface, the interpretation of the procedure in (16) is more complicated.

Generally speaking, the term $R_0 + R$ in the argument of the function a is time-dependent due to the transmitter and receiver motions. However, this effect can be ignored if velocities $\vec{V}_t$ and $\vec{V}_r$ are small enough. This means that a surface within an area significant for the integration should be regarded as unchanged or "frozen" during the time integration T_i. Therefore, upon substituting (5) into (16), we can change the order of the integrations and obtain the following result for an instantaneous signal:

$$Y(t_0,\tau) = T_i \int D(\vec{r})\chi[t_0, \delta\tau(\vec{r}); \delta f(t_0+\tau)] \times g(\vec{r}, t_0+\tau)\, d^2r, \tag{17}$$

where

$$\chi[t_0,\delta\tau;\delta f] = \frac{1}{T_i}\int_0^{T_i} a(t_0+t')a[t_0+t'+\delta\tau] \times \exp[-2\pi i \delta f t']\, dt' \tag{18}$$

and

$$\delta\tau(\vec{r}) = \tau - [R_0(\vec{r}) + R(\vec{r})]/c; \quad \delta f(t_0+\tau) = f_D(t_0+\tau) - f_c. \tag{19}$$

The function χ is known in radar pulse-compression techniques as the Woodward Ambiguity Function (WAF) of pseudo-random sequences (cf., [14], [23], [24]). Because the function χ plays a very important role in any further analysis, we consider it in more detail. First of all, we shall assume that the Doppler frequency does not change significantly over time $\tau \sim (R_{0,\mathrm{sp}} + R_{\mathrm{sp}})/c$. Therefore, we can set $f_D(t_0+\tau) \approx f_D(t_0)$, and $\chi[t_0,\delta\tau(\vec{r});\delta f(t_0+\tau)]$ turns into $\chi[t_0,\delta\tau(\vec{r});\delta f(t_0)]$. Note that time t_0 enters into the function χ as a parameter reflecting a dependence of the Doppler frequency $f_D(t_0)$ on the instantaneous velocities of both the transmitter and receiver. Thus, for brevity, we shall refer to χ as the function of two variables $\chi(\delta\tau, \delta f)$.

It is impossible to obtain a general analytical expression for this function, because the functions $a(t)$ under the integral are pseudo-random sequences of $+1$ and -1. Some numerical and empirical results for the WAF are known in literature (cf., [14], [24], [25]). Here, we assume a simple model for $\chi(\delta\tau, \delta f)$, which relies on its analytical behavior along the temporal and frequency axes. Indeed, $\chi(\delta\tau, \delta f)$ at $\delta f = 0$ transforms into a known function $\Lambda(\delta\tau)$ [12]

$$\Lambda(\delta\tau) \equiv \chi(\delta\tau, 0) = \frac{1}{T_i}\int_0^{T_i} a(t_0+t')a(t_0+t'+\delta\tau)\, dt' = \begin{cases} 1 - |\delta\tau|/\tau_c, |\delta\tau| \le \tau_c(1+\tau_c/T_i) \\ -\tau_c/T_i, |\delta\tau| > \tau_c(1+\tau_c/T_i), \end{cases} . \tag{20}$$

The triangular shape of this function at $|\delta\tau| \le \tau_c(1+\tau_c/T_i)$ is due to overlapping of two identical rectangular "chips" from $a(t)$ and from the shifted function $a(t+\delta\tau)$. For $|\delta\tau| > \tau_c(1+\tau_c/T_i)$, the result $-\tau_c/T_i$ follows from peculiar properties of so-called maximal length codes used in GPS, in which the number of "$-$" in $a(t)$ exceeds the number of "$+$" by one (cf., [12], [26])., since $\tau_c \ll T_i$. We can always replace $-\tau_c/T_i$ in (20) with 0 for further calculations.

Along the frequency axis (i.e., when $\delta\tau = 0$), $\chi(\delta\tau, \delta f)$ transforms into another known function due to the code property $a^2(t) \equiv 1$)

$$S(\delta f) \equiv \chi(0, \delta f) = \frac{1}{T_i}\int_0^{T_i} \exp(-2\pi i \delta f t')\, dt' = \frac{\sin(\pi\delta f T_i)}{\pi\delta f T_i}\exp(-\pi i \delta f T_i). \tag{21}$$

In what follows, we assume similarly to [27], that the function χ can be approximated by the following factorized form:

$$\chi(\delta\tau, \delta f) = \Lambda(\delta\tau)S(\delta f). \tag{22}$$

Note that (22) describes the function $\chi(\delta\tau, \delta f)$ adequately only in narrow zones along axes $\delta\tau = 0$ and $\delta f = 0$. However, these are zones where $\chi(\delta\tau, \delta f)$ reaches its maximum value. Therefore, we expect that these zones are most significant for integration in (17). Of course, an accuracy estimation would be helpful along with the search for a more accurate approximation for $\chi(\delta\tau, \delta f)$.

By making use of (22), we can rewrite the instantaneous signal from (17) in the following form:

$$Y(t_0,\tau) = T_i \int D(\vec{r})\Lambda[\delta\tau(t_0,\vec{r})]S[\delta f(t_0,\vec{r})]g(\vec{r},t_0)\, d^2r. \tag{23}$$

According to (20), the function Λ includes in the integration in (23) only that part of a surface $\Delta\Sigma$ that satisfies the condition $|\tau - (R_0+R)/c| < \tau_c$. It follows from the fact that the signal Y received at the time delay τ is formed by only those radio waves that could be scattered by points located on an ellipsoid of rotation having the transmitter and the receiver as its foci. That means that all these scattered waves will experience the same time delay. The intersection of this ellipsoid with the plane surface is an ellipse. Elliptic boundaries of the area $\Delta\Sigma$ satisfying the condition $R_0 + R = \mathrm{const}$ are called iso- or equirange lines. Therefore, the area $\Delta\Sigma$ should have the shape of an elliptical ring (an annulus zone), which sweeps the surface as time delay τ increases.

The function $|S(\delta f)|$ is centered near $f_{\mathrm{D}} = f_c$, concentrating mostly within the area $|f_c - f_{\mathrm{D}}| \sim 1/2T_i$. Recall that $f_D = f_{D,0} + f_s$, and $f_s \approx q_z v_z/2\pi$. Assuming a complete compensation for $f_{D,0}$ in a case of normal incidence, we obtain $\delta f T_i/2 \approx v_z T_i/\lambda$. For $T_i = 1$ ms, $\lambda = 0.19$ m, and $v_z = 1$ m/s, we obtain that $|S| = 0.9998$. For $T_i = 10$ ms, we obtain 0.984. Therefore, even under these rather severe conditions, the effect of orbital motions is negligible, and it suffices to account only for velocities of the transmitter and the receiver with respect to the Earth's surface. These velocities via function $|S[\delta f(\vec{r})]|$ determine Doppler zones significant for the integration in (23). The boundaries of these zones can be found from the equation

$$f_c \pm \frac{1}{2T_i} = [\vec{V}_t \cdot \vec{m}(\vec{r}) - \vec{V}_r \cdot \vec{n}(\vec{r})]/\lambda. \tag{24}$$

Scatterers that are positioned on a certain line described by (24) provide equi-Doppler returns. At this point, one can notice an

analogy between our bistatic GPS scatterometer and a mapping synthetic aperture radar (SAR) [28]. Indeed, in our case, we have the same Doppler frequency/time delay format and pixels formed by the intersection of equi-Doppler lines and equi-distance lines. The only difference is that the geometry of these lines is more complex due to the bistatic configuration. In our case, the equi-distance line is an ellipse on a plane (rather than a circle as in the SAR case), and the equi-Doppler line, strictly speaking, is the curve of a higher order than a hyperbola (which is the case for the SAR). However, in some instances, it can be approximated by a hyperbola. For example, if the first term in the right-hand side of (24) does not change significantly compared to the second one (or vice versa), so it can be replaced by a constant value, then (24) turns into a hyperbola equation.

C. Time-Delayed GPS Scattered Signal Power

The output of the GPS receiver is the average power as a function of the delay τ obtained by squaring in-phase and in-quadrature components of the signal and then averaging over the accumulation time T_a

$$\langle |Y(\tau)|^2 \rangle = \frac{1}{T_a} \int_0^{T_a} |Y(t_0, \tau)|^2 \, dt_0. \tag{25}$$

In practice, the above average is obtained by the sample averaging

$$\langle |Y(\tau)|^2 \rangle = \frac{1}{N} \sum_{j=1}^{N} |Y(t_{0,j}, \tau)|^2 \tag{26}$$

where maximal $N = T_a/T_i$, and j is the number of a sample obtained by the correlation procedure in (16) and assigned to the time moment $t_{0,j}$ within the interval T_a. T_a should be greater than T_i and greater than the correlation time of the random variations of the signal $|Y(t_0, \tau)|^2$ caused by the scattering process. This condition would allow us to use an ensemble average over surface statistics for the theoretical modeling of $\langle |Y(\tau)|^2 \rangle$.

As shown in Appendix A, $\langle |Y|^2 \rangle$ as a function of time delay (for brevity, we hereafter call it a waveform) is given by

$$\langle |Y(\tau)|^2 \rangle = T_i^2 \int \frac{|\Re|^2 D^2(\vec{\rho}) \Lambda^2[\tau - (R_0 + R)/c]}{4 R_0^2(\vec{\rho}) R^2(\vec{\rho})} \times |S[f_D(\rho) - f_c]|^2 P\left(-\frac{\vec{q}_\perp}{q_z}\right) \frac{q^4}{q_z^4} \, d^2\rho. \tag{27}$$

One can see that the main contribution to the integral in (27) comes from the area limited by intersection of four spatial zones. These are the power antenna-footprint defined by the D^2-function, the annulus zone defined by the Λ^2-function, the Doppler zone defined by the $|S|^2$-function, and the glistening zone defined by the probability distribution function (PDF) P of surface slopes pertinent for reflection. The width of the entire annulus zone and the thickness of its ring depend on the time delay τ and the bistatic geometry, whereas the width of the glistening zone carries information about ocean wave slopes or a near-surface wind. This geometry is depicted in Fig. 2. The smallest annulus zone occurs at a time delay corresponding to the nominal specular point. For larger time delays the annulus becomes

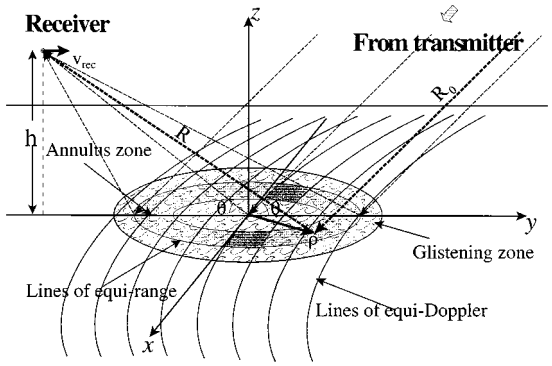

Fig. 2. Configuration of glistening, annulus, and Doppler zones.

larger in diameter (and more narrow) until it finally leaves the glistening zone. It is clear that the waveform $\langle |Y(\tau)|^2 \rangle = 0$ for time delays τ shorter than $(R_{0,\mathrm{sp}} + R_{\mathrm{sp}})/c - \tau_c$ (see (8) and (9)). Therefore, it is convenient to introduce the offset time delay $\tau_0 = \tau - (R_{0,\mathrm{sp}} + R_{\mathrm{sp}})/c$.

From (27), it follows that changes in wind conditions produce variations in P, and this affects the behavior of the waveform $\langle |Y(\tau_0)|^2 \rangle$ as a function of time delay τ_0. Therefore, by measuring this dependence, one would be able to draw conclusions about the wind speed at the ocean surface. However, other functions in the integrand of (27) also play an important role and can affect the final result.

Consider first the role of the Doppler effect on scattered power described by the function $|S|^2$ in (27). As was mentioned above, the average Doppler shift has little importance because it can be compensated routinely by the GPS receiver. More important is to what extent the Doppler shift changes over the glistening zone, or how large the Doppler spreading is: positive, $\Delta f_D^+ = f_{D,\max} - f_{D,\mathrm{sp}}$ and negative $\Delta f_D^- = f_{D,\mathrm{sp}} - f_{D,\min}$. Here, $f_{D,\mathrm{sp}}$ corresponds to the Doppler shift for radio waves reflected from the nominal specular point. If $\Delta f_D^+ + \Delta f_D^-$ is smaller than the Doppler bandwidth $\Delta f_0 = 1/2T_i$, then the Doppler spreading has little impact on the waveform $\langle |Y(\tau)|^2 \rangle$. In other words, if the size of an entire glistening zone is smaller than the width of the Doppler zone described by the function $|S|^2$, then $|S|^2$ can be replaced by unity in (27), and Doppler effects can be neglected.

In Fig. 3, we demonstrate the Doppler shift of the received signal as a function of the scatter location on the surface along coordinate y $(x = 0)$ for the case when both receiver and transmitter are moving within the incident plane in the positive y-direction. The altitude of the receiver is 3 km, and the velocity is 0.15 km/s. Curves from top to bottom correspond to different values of the transmitter elevation angle θ. Horizontal lines correspond to $f_{D,\mathrm{sp}}$ for each elevation angle θ. The average Doppler shift is minimal (zero) for normal incidence. It increases in absolute value with decreasing θ. Now, assuming that $T_i = 1$ ms, we have $\Delta f_0 = 1/2T_i = 500$ Hz, which is smaller than $\Delta f_D^+ = |\Delta f_D^-| \approx 900$ Hz. Therefore, in the case of normal incidence the function, $|S|^2$ would cut the contribution to the integral due to both large Δf_D^+ and Δf_D^-. At the same time, at $\theta \leq 40°$ (even though Δf_D^- is too large) at least $\Delta f_D^+ \ll \Delta f_0$, so $|S|^2 \approx 1$ in the area of positive y, and this would preserve about half of the scattered power. This behavior is clearly seen

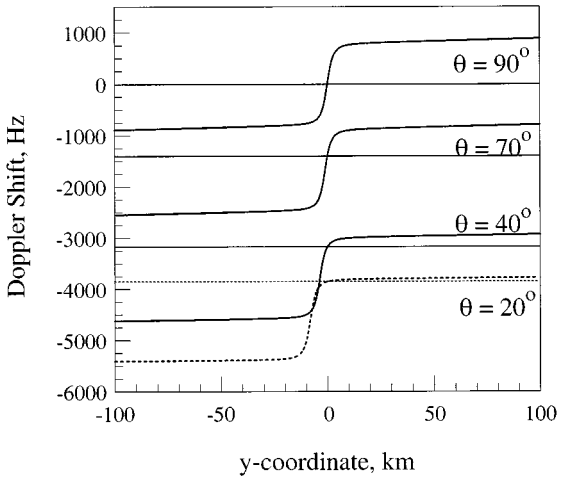

Fig. 3. Doppler shift along longitudinal coordinate for different elevation angles.

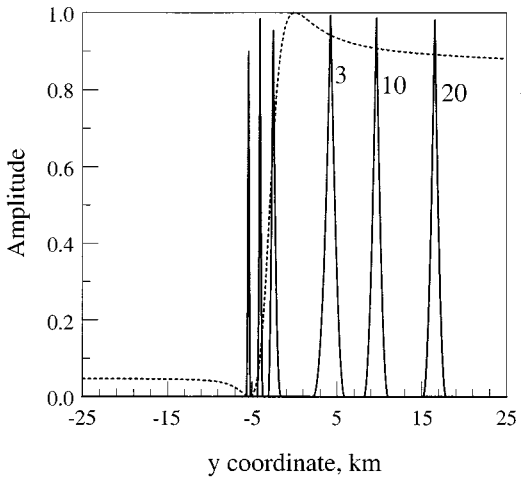

Fig. 5. Relative position of Doppler zone function (dashed curve) and annuli at different time delays for $\theta = 45°$.

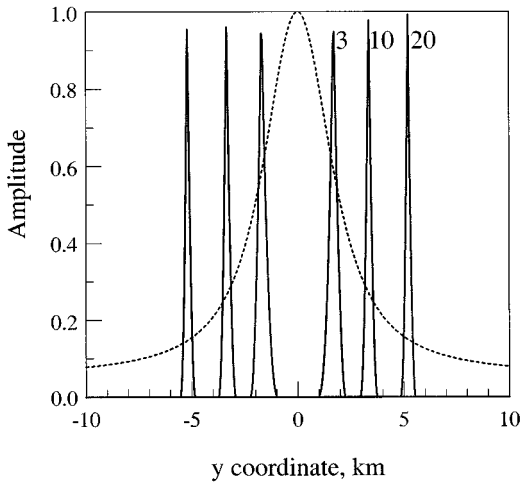

Fig. 4. Relative position of Doppler zone function (dashed curve) and annuli at different time delays for $\theta = 90°$.

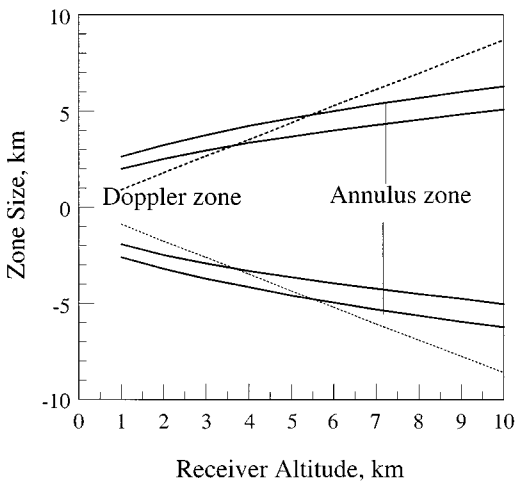

Fig. 6. Size of Doppler and annulus zones as a function of the receiver altitude for $\theta = 90°$.

in Figs. 4 and 5, where Λ^2- and $|S|^2$-functions are shown along the y-coordinate for $\theta = 90°$ and $\theta = 40°$. Annuli for 3, 10, and 20 half-chip delays are seen as sharp peaks compared to the relatively smooth Doppler-zone function. Note that the scattered signal comes from two intersections of the annulus zone and the Doppler zone, assuming that both of them are within the glistening zone. Fig. 5 demonstrates an asymmetric form for the $|S|^2$-function at $\theta = 45°$compared to the symmetric one in Fig. 4 for the normal incidence case. The dependence of the size of the Doppler and annulus zones, taken at the ten half-chip time delay, as a function of the receiver altitude (for 0.15 km/s aircraft velocity) is depicted in Fig. 6 for relatively low receiver altitudes (up to 10 km). It is seen that the size of the Doppler zone grows faster than that of the annulus zone and eventually exceeds it. This indicates that airplane flights at higher altitudes are more favorable. However, a transition to satellite altitudes and velocities reverses the situation: the Doppler zone becomes much narrower than the corresponding annulus zone. This would result in a significant reduction of the received power of the scattered signal. Therefore, additional measures should be taken to improve the performance of a GPS scatterometer working in orbit.

From the analysis of the Doppler spreading, the following conclusions can be drawn. For aircraft altitudes and velocities, the Doppler zones are relatively wide compared to the size of the glistening zone, and the SNR is relatively high. As is shown below, the situation that occurs when Doppler effects can be minimized allows us to use a more optimal scheme of wind retrieval. This minimization can be done by an appropriate reduction of the integration time T_i with an acceptable loss of the SNR. In the case of satellite altitudes and velocities, a similar approach may not help because the SNR is already too low. Therefore, a significant reduction of T_i could lead to an additional decrease of the SNR.

For the case of omnidirectional receiving antenna ($D^2 = 1$), (27) has been used for numerical simulations that have resulted in curves presented in the next section. The double integral in (27) cannot be calculated analytically for arbitrary elevation angles even in the case of the simplified isotropic PDF of slopes, P. Because of this, we rely here mainly on numerical evaluations of this integral. However, there is a situation when certain analytical estimations of (27) are possible. This happens when a bistatic configuration degrades into a monostatic one. As shown

in Appendix C, for the case of the GPS transmitter close to the zenith, a wide enough Doppler bandwidth Δf_0, and Gaussian isotropic PDF of slopes P described by a single slope variance parameter σ_s^2, the waveform takes the following simple form:

$$\langle |Y(p_0)|^2 \rangle = \frac{T_i^2 A(p_0)}{h_0^2 \sigma_s^2} \exp\left\{ -\frac{b(p_0)}{\sigma_s^2} \right\} \tag{28}$$

where dimensionless functions $A(p_0)$ and $b(p_0)$ are explicitly given by (63) and (64), $p_0 = c\tau_0/h$ is a nondimensional offset time delay, and h_0 and h are altitudes of the transmitter and the receiver, respectively.

The expression in (28) is rather convenient for quick estimations of the σ_s or wind speed from measurements of $\langle |Y(p_0)|^2 \rangle$ as a function of the time delay τ_0. Indeed, the value $Q(p_0) = \langle |Y(p_0)|^2 \rangle h_0^2 / T_i^2 A(p_0)$ obtained from (28), (63), and (64) does not depend on h_0 and h, and depends only on σ_s^2 and the parameter p_0. In a logarithmic scale, it becomes

$$\log Q(p_0) = -\log \sigma_s^2 - b(p_0) \log e / \sigma_s^2. \tag{29}$$

A plot of $\log Q(p_0)$ with respect to $b(p_0)$ is a straight line with slope $-\log e/\sigma_s^2$. The function $b(p_0)$ changes monotonically with increasing p_0: $b(p_0) \approx p_0/2$ for $p_0 \ll 1$, and it saturates to unity for $p_0 \gg 1$, so there is a one-to-one correspondence between p_0 and b. Recall that (29) describes the behavior of the descending part of the waveform, or the trailing edge. Therefore, σ_s or wind speed can be quickly estimated by measuring slopes of trailing edges of experimental waveforms transformed according to (29). A direct comparison between numerically calculated and the analytical curves presented in the next section shows limits of this approach. The similarity with airborne radar altimetry [20], [22] stems from the cylindrical symmetry of the problem geometry both for the radar altimetry method and for the near-zenith case considered here. Only in this case do the functions Λ^2 and P not depend on azimuthal angle. This reduces the azimuth angle integration to a 2π factor. However, from a geometrical point of view there is one difference. In the altimetry case we have a pure monostatic configuration when both transmitter and receiver are collocated, so the scattered wave travels exactly in the opposite direction with respect to the incident one. In the GPS case the transmitter is separated from the receiver by a significant distance, about 20 000 km. Therefore, incident and scattered waves travel along different paths.

Despite using the delta-function approximation for Λ^2 in (60), this approach demonstrates good reliability for typical experimental conditions, especially for a receiver altitude h of 5 km and higher. This approximation works well when the thickness of the annulus zone, $\Delta\rho_\Lambda(\tau_0)$ is smaller than the glistening zone size ρ_P, and $\Delta\rho_\Lambda(\tau_0)$ decreases as τ_0 increases. Let us roughly estimate the scales of functions Λ^2 and P for the GPS transmitter at the zenith at altitude $h_0 \approx 20\,000$ km. The scales are: $\Delta\rho_\Lambda \approx \sqrt{2c\tau_c h}(\sqrt{\tau_0/\tau_c + 1} - \sqrt{\tau_0/\tau_c - 1})$, and $\rho_P \approx h\sigma_s/\sqrt{\log e/2}$ at -20 dB level (we assume here $\tau_0 = 5\tau_c; \sigma_s = 0.1$). Estimations for these scales are presented in Table I. This table demonstrates that for altitude about 5 km, the value ρ_P starts dominating over $\Delta\rho_\Lambda$, because $\Delta\rho_\Lambda$ grows proportionally to $\sqrt{h}$, while ρ_P is proportional to h.

TABLE I
SCALES OF ANNULUS AND GLISTENING ZONES

h, km	1	5	10	50	100	500
$\Delta\rho_\Lambda$, km	0.35	0.78	1.10	2.46	3.48	7.77
ρ_P, km	0.21	1.07	2.15	10.7	21.5	107

IV. NUMERICAL SIMULATIONS OF WAVEFORMS

To investigate potentialities of the discussed technique we have performed numerical simulations of waveforms $\langle |Y(\tau_0)|^2 \rangle$. For the calculations, we have used the Gaussian statistics of sea surface slopes, with anisotropic wind-dependent surface-slope variances. These variances can be derived from any appropriate sea surface spectrum on which spectral-peak position depends on the wind. Comparing results obtained with different spectra is beyond the scope of this paper. We have chosen the directional spectrum by Elfouhaily *et al.* [31], presented in Appendix B by (48)–(55). According to the physical meaning of the two-scale surface model, the needed variations and correlations were obtained by completing the numerical integration in (41)–(43) over wave numbers smaller than $2\pi(3\lambda)^{-1}$ [15], [21], where $\lambda = 0.19$ m for L1 GPS carrier.

The polarization-dependent reflection coefficient $\Re$ has been calculated from (37) for the right-hand circular polarization (RHCP) of the transmitted signal and the left-hand circular polarization (LHCP) of the received signal using a typical value for the dielectric constant of sea water $\varepsilon = 73.0 + i57.5$ for $\lambda = 0.19$ m. In recent airborne experiments on GPS ocean scattering [6], an LHCP low-gain antenna was used. This was a well-justified choice because, as calculations show, the scattered signal on the opposite RHCP (the polarization transmitted by the satellites) is much lower for steep and moderate elevation angles. But for low-grazing angles, signals on RHCP and LHCP start to converge. The low-gain type of antenna mentioned above allowed us to use the reasonable assumption $D(\vec{\rho}) \equiv 1$ in calculations. In order to express results in relative values, we performed numerical calculations of the waveform (as a function of an offset time delay τ_0) normalized by the direct signal $\langle |Y(\tau_0)|^2 \rangle R_d^2/T_i^2$, where R_d is the distance between the GPS satellite and the receiver, and coherent time integration T_i is 1 ms. The units for the time delay τ_0 are half-chips $\tau_c/2 = 0.5\ \mu$s.

The first series of curves obtained by a numerical integration of (27) demonstrate (a) a sensitivity of waveforms to wind conditions and (b) the evolution of waveforms with changing altitude of the GPS receiver. Fig. 7 demonstrates a sensitivity of waveforms to the wind direction for aircraft altitude $h = 10$ km, GPS elevation angle $\theta = 45°$, and wind speed $U = 10$ m/s. The waveforms in their near-peak part exhibit a low wind-direction dependence. For the lower part of waveforms, this dependence is more pronounced, and the difference between upwind and cross-wind waveforms amounts to 3 dB at the time delay of 24 half-code lengths. This relatively low sensitivity to wind direction is a result of a strong averaging of azimuthal dependencies of anisotropic PDF of slopes P during the integration over the annulus zone.

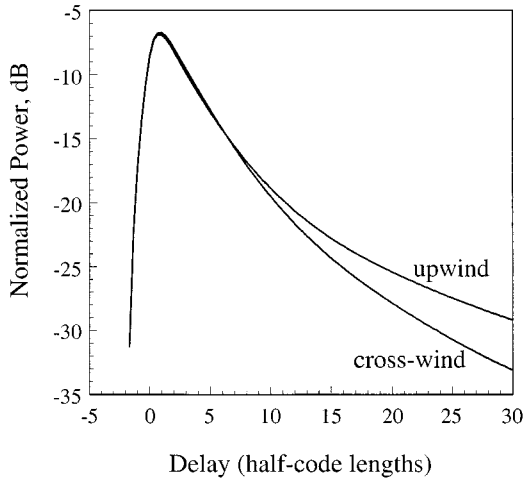

Fig. 7. Waveforms for upwind and cross-wind directions ($\theta = 45°$, $h = 10$ km, and $U_{10} = 8$ m/s).

The sensitivity to wind speed can be seen in Fig. 8(a)–(c). The waveforms were calculated for various winds but for the same GPS elevation angle $\theta = 45°$ and for the 0° wind direction. For Figs. 8(a) and (b), we assume that the GPS receiver is on board an airplane moving with speed $v_{\rm rec} = 0.17$ km/s in the same plane and direction as the GPS satellite having speed $v_{\rm tr} = 3.87$ km/s. Estimations of the $|S|^2$-function indicate that for this altitude the effect of Doppler spreading is negligible. Fig. 8(a) shows that at $h = 1$ km and wind speed 4 m/s, the waveform is close to that for the direct signal (i.e., to annulus function Λ^2 itself) except for the part of the trailing edge below -20 dB. The increase of wind up to 10 m/s results in practically no change in the leading edge of the waveform and in a rather modest lift of the trailing edge above the level of -20 dB. This happens because at altitudes that are too low, the glistening zone is smaller than the annulus zone.

Curves in Fig. 8(b) obtained for $h = 10$ km demonstrate much more interesting behavior. First, notice that the peak value of the waveform decreased by several decibels compared to the case of $h = 1$ km. Secondly, this peak value starts to show a dependence on wind speed. But more important is that negative slopes of the trailing edge acquired a more pronounced sensitivity to the wind speed than for $h = 1$ km. The behavior of the peak and the behavior of the slopes are closely connected. It simply manifests the redistribution of the scattering energy over the glistening zone. Stronger winds create a rougher surface and a wider glistening zone with less reflectivity from the vicinity of the nominal specular point and vice versa. The smaller the slopes of the waveform, the stronger are the winds. However, with wind increase the difference between corresponding slopes becomes less distinctive. This is a result of the approximately logarithmic dependence of σ_s^2 on U. Any wind remote sensing technique that relies on wave slopes has this type of limitation. Note that the effect of Doppler spreading for $h = 10$ km and $v_{\rm rec} = 0.17$ km/s is still rather small.

Our primary goal was to develop a theoretical framework for the GPS sea-surface wind-measurement technique from board an airplane. However, it is instructive to test our model assuming

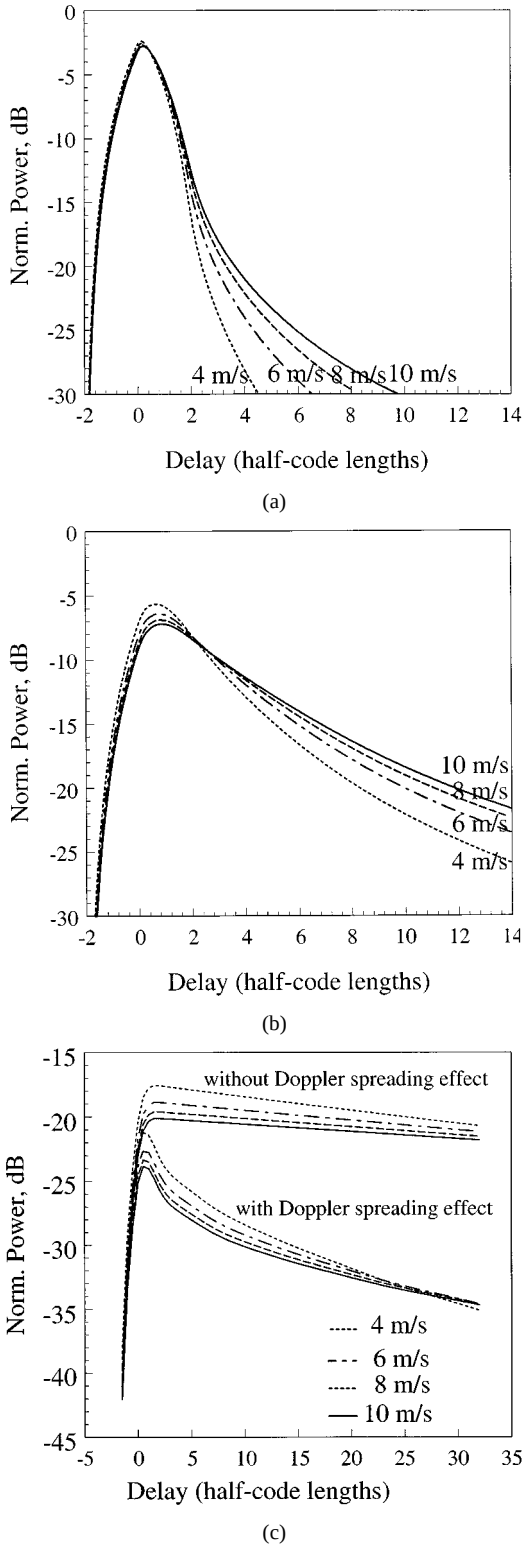

Fig. 8. Waveforms for various receiver altitudes and wind speeds at $\theta = 45°$: (a) $h = 1$ km, (b) $h = 10$ km, and (c) $h = 300$ km.

that the scattered GPS signal is supposed to be detected from a satellite orbit. To compare how waveforms are changing as a result of significant increase of the receiver altitude and its speed (as for the case of a satellite-borne receiver) we performed calculations, assuming the same omnidirectional antenna pattern, for $h = 300$ km and $v_{\rm rec} = 7.7$ km/s, which are pre-

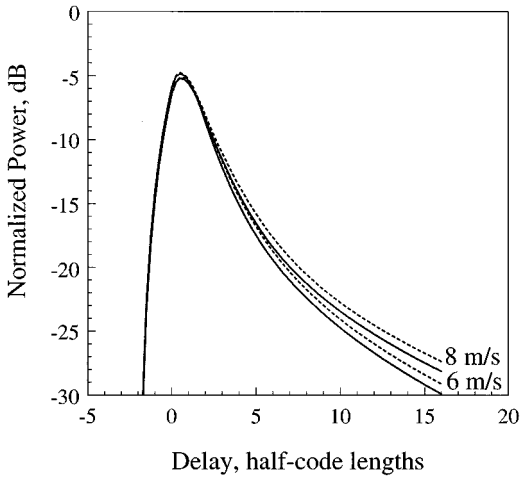

Fig. 9. Comparison between curves obtained for $h = 5$ km, $\theta = 45°$, and $v_{\rm rec} = 0.17$ km/s, taking into account Doppler spreading (solid curves) and without it (dashed lines).

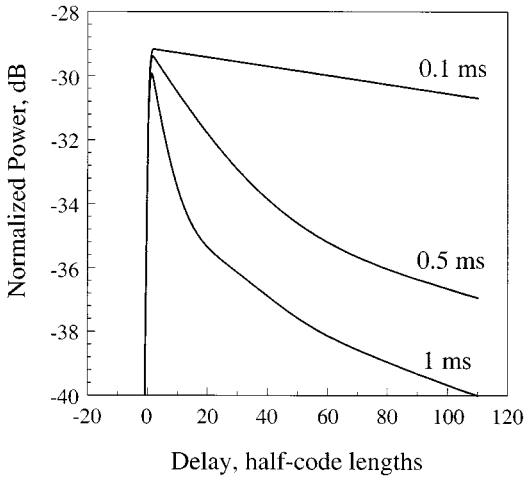

Fig. 10. Comparison between curves obtained for $h = 225$ km, $v_{\rm rec} = 7.9$ km/s, $U_{10} = 8$ m/s, $\theta = 45°$, $\tau_c = 0.1$, μs (the P-code) and different integration times T_i.

sented in Fig. 8(c). The main differences are significantly lower peak power, and a rather steep fall of trailing edges for different winds with their convergence at large time delays. The first effect is due to the factor $1/R^2$, which starts to be noticeable at these altitudes, and the second is a result of a significantly stronger Doppler spreading effect resulting in narrowing of the $|S|^2$-function compared to the glistening zone. Without accounting for this effect, the trailing edges would go almost horizontally, reflecting the significantly stretched linear size of the glistening zone due to high altitudes.

To show to what extent the Doppler spreading can affect the performance of airborne GPS receivers, we calculated waveforms with the Doppler spreading effect, and without it for $|S|^2 = 1$, $h = 5$ km, $v_{\rm rec} = 0.17$ km/s, and for two winds: $U = 6$ m/s and $U = 8$ m/s. Other parameters were the 0° wind direction; the GPS elevation angle $\theta = 45°$, and the airplane is moving in the same direction as the GPS satellite. Curves in Fig. 9 represent waveforms with (solid curves) and without (dashed curves) taking into account the Doppler spreading. It is seen that the influence of the Doppler spreading on waveforms increases with the time delay. However, for these aircraft altitudes and velocities the Doppler spread produces a rather minor effect. A transition to satellite altitudes with actual satellite velocities considerably changes the situation. The Doppler spread increases significantly, which leads to the much narrower Doppler zone with respect to the glistening zone. This manifests itself through decrease of peak power and steepening of the trailing edge, which is clearly seen in Fig. 8(c).

Above we presented results for the C/A code with $\tau_c = 1$ μs and with the coherent integration time $T_i = 1$ ms. For comparison we considered the case of a satellite receiver at $h = 225$ km working with the P-code ($\tau_c = 0.1$ μs). In Fig. 10, three waveforms are presented, which correspond to different integration times ($T_i = 1$ ms, 0.5 ms, 0.1 ms) for fixed wind speed $U_{10} = 8$ m/s and elevation angle $\theta = 45°$.

Finally, we compare results obtained using the analytical model and the direct numerical computations. For moderate altitudes from about 5 km and higher and elevation angles close to $\theta = 90°$, the analytical model in (29) is in close agreement with the waveform trailing edge from the numerical model. This is seen in Figs. 11(a) and (b), where we compare results for the function $Q(p_0)$ obtained by a direct numerical integration of (27) and from the analytical model for $h = 5$ km and different wind conditions. The $\log Q(p_0)$ is plotted against the parameter $b(p_0)$ nonlinearly related to the nondimensional delay p_0. With these coordinates, the trailing edges of the waveforms transform into straight lines. This behavior is similar to that observed in waveforms obtained by means of airborne radar altimetry [20], [22]. Remember that a trailing edge of both altimetric pulse-waveforms and GPS waveforms depends on surface roughness that, in turn, is influenced by the surface wind field. Fig. 11(a) corresponds to the case of normal incidence ($\theta = 90°$), and Fig. 11(b) shows results obtained for the angle $\theta = 60°$. For normal incidence the approximate solution in the form of straight lines agrees very well with the trailing edges of $\log Q(p_0)$. For elevation angles between 90° and 60° the numerical curves gradually depart from analytic approximations represented by the straight lines. For low wind of 4 m/s we can see some offset between numerical waveforms and analytical ones. However, the absolute value of the waveform has no significance for wind retrieval. What matters is the slope of the waveform trailing edge. As it seen from Fig. 11(b), analytical dependencies follow slopes of the numerical waveforms in their near-peak part of the trailing edge even for low winds. For elevation angles smaller than 60°, the departure from cylindrical symmetry becomes significant, and the only way to study waveforms is to perform the direct numerical integration in (27).

V. Discussions and Conclusions

A robust, theoretical model that describes the power of the scattered GPS signal as a function of geometrical parameters and wind has been developed. The core of this model is a bistatic radar equation derived using the geometric optics limit of the Kirchhoff approximation within the framework of the two-scale surface model. This equation represents an integral over the scattering surface which includes a normalized cross section of

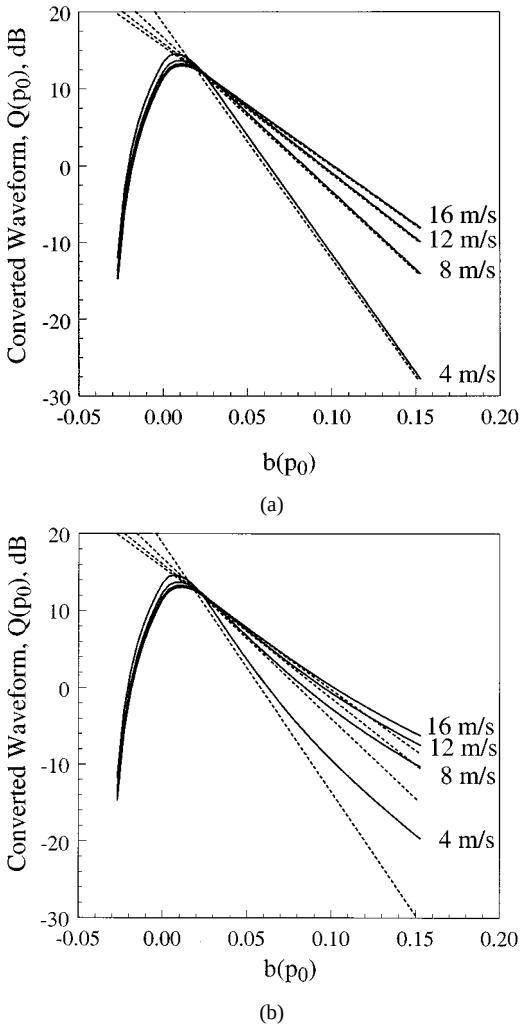

Fig. 11. Comparison between analytical asymptotes (dashed lines) and numerical calculations (solid curves): (a) $\theta = 90^\circ$ and (b) $\theta = 60^\circ$.

the rough surface based on the wave-slope probability density function, a polarization-dependent reflectance coefficient, and a footprint factor. Numerical simulations of this equation give the power level of the scattered signal (a waveform) as a function of the time delay, the elevation angle of the GPS satellite, the height of the receiver, and surface wind speed/direction. In some regimes an analytical solution for the bistatic radar equation is possible. This solution transforms the trailing edges of the waveforms into a set of straight lines that offer a convenient method for quick wind speed estimations. The treatment of Doppler effects within the model revealed the similarity of this technique with the synthetic aperture radar.

The curves presented in Figs. 8(a)–(c) for aircraft altitudes and velocities indicate that altitudes within the interval 5–15 km are the best for inferring wind speed from trailing edge slopes. With the fixed width of the annulus zone, the glistening zone is too narrow at lower altitudes and too wide at higher altitudes. Another negative factor of high altitudes is a significant reduction of peak power with increasing altitude. The sensitivity of the waveforms to the wind direction for all altitudes is noticeable only for rather low parts of trailing edges. A transition to satellite altitudes (even low ones) together with satellite velocities makes the peak power reduction and the Doppler spreading effect a significant problem.

The first problem might be solved by using a high-gain receiving antenna. Note, also, that in order to work with different GPS satellites (i.e., with different glistening zones) this antenna should have a scanning mechanism. In this paper we assumed the low-gain type of antenna allowing us to consider the footprint function $D(\vec{\rho})$ as a constant. For high-gain antennas, generally speaking, one needs to keep this function of $\vec{\rho}$ under the integral in (27). This does not make calculations more difficult. In order to detect the effect of wind on the trailing edge of waveforms, the antenna beam width should be wider than an angular extent of the glistening zone, and the antenna should be directed toward a nominal specular point on the sea surface. Otherwise, the trailing edge would be significantly cut off by the antenna beam pattern. This condition, of course, put a limitation on a maximal antenna gain, and therefore, on an capability to significantly increase the peak power of waveforms. On the other hand, the detection of the trailing edge with the antenna beam narrower than the glistening zone would require an ability to perform a fast scanning within the glistening zone.

Here, we considered a fixed value of the Doppler compensating frequency (related to the nominal specular point), which establishes only one specific Doppler zone on the scattering surface going through the center of the glistening zone. That highlights peaks and suppresses trailing edges of waveforms, diminishing wind impact on them. By going through a wide enough interval of compensating frequencies, one can restore slopes of these trailing edges with wind-related information assuming that other problems mentioned above are solved. These examples show that the future space-borne systems should get special attention in terms of hardware system design.

The airborne experimental techniques (developed at NASA/LaRC) [6] have been limited by measurements of the waveforms of the scattered GPS signal (i.e., of the scattered power as a function of the time delay). Different time delays correspond to different size annulus-like footprints that emerge from the code structure of the GPS signal. Now assume that one is able to generate a narrow enough Doppler zone with a position determined by the compensation frequency. The intersection of an elliptical annulus with this Doppler zone would form a spatial cell that discriminates the scattered signal from a smaller area of sea surface than before, both in radial and azimuthal directions. This GPS delay-frequency mapping technique having much in common with the SAR mapping technique, should allow measurements of wind velocity and wind direction with higher accuracy then the delay-mapping technique considered in this paper.

In the present study, we limited ourselves to the single-point Gaussian statistics of surface elevations and surface slopes. However, stricter requirements on the accuracy of the wind retrieval, or measurements in low-grazing-angle regimes demand a more realistic surface model that could include features of non-Gaussian, multivariate, anisotropic statistics. To develop our model we have chosen the geometrical optics limit of the Kirchhoff approximation (within the framework of the two-scale surface model) due to its physical simplicity and the sufficient accuracy for considered experimental conditions.

Notice that limitations brought by the Kirchhoff approximation are needed mostly for the derivation of the bistatic cross section σ_0 in the form of (32) rather than for the derivation of the bistatic radar equation given by (31). This equation can be obtained rigorously using the technique of scattering amplitudes [19] even without specifying the concrete way of calculation the bistatic scattering cross section σ_0. The cross section itself can be obtained more accurately using the Small Slope Approximation (SSA) [32] (or other unifying theories [33]) that embraces both the quasispecular and Bragg types of scattering and does not require introducing an ambiguous scale-dividing parameter inherent to the two-scale scattering model. Calculations [34] show a good fit between results for the LHCP signal obtained using both the SSA and the Kirchhoff approximation for scattering angles smaller than $\pm 30^\circ$ around the nominal specular direction. For the LHCP signal a departure takes place for wider scattering angles, outside the glistening zone, where the contribution from quasispecular reflections rapidly decreases, so the contribution from Bragg scattering cannot be neglected. Notice that, in contrast to the Kirchhoff approximation, the SSA calculations for the RHCP signal demonstrate that Bragg scattering contributes to the signal even at the specular direction. However, the detection of this type of scattering in bistatic GPS experiments requires more sensitive receivers.

Appendix A
Radar Equation for Time-Delayed Scattered Power

To proceed further with calculations of $\langle |Y(\tau_0)|^2 \rangle$, we need to make additional simplifications in (5) and (6). To extract the large-scale elevation $\zeta(\vec{r}, t)$ in an explicit form we expand functions in the integrand into the Taylor series over ζ, withholding zero-order terms in slow functions $\Re$, D, a, and $1/R_0R$ and first-order terms in the exponent. Doing this in $1/R_0R$ we produce an error smaller than value $k\sigma_\zeta^2/\min(R_0, R) \ll 1$, and for a this introduces an error smaller than $\sigma_\zeta/c\tau_c \ll 1$. Using this approximation results in the following expression for the time-delayed average power:

$$\begin{aligned}\langle |Y|^2 \rangle &= T_i^2 \int \langle (D\Lambda S g)'(D\Lambda S^* g^*)'' \rangle \, d^2r' \, d^2r'' \\ &= \frac{T_i^2}{16\pi^2} \int \Phi(\vec{r}', \vec{r}'') \left(\frac{D\Lambda S \Re q^2}{R_0 R q_z} \right)' \left(\frac{D\Lambda S^* \Re^* q^2}{R_0 R q_z} \right)'' \\ &\quad \times \exp[iK(R_0' + R' - R_0'' - R'')] \, d^2r' \, d^2r''. \end{aligned} \tag{30}$$

Now $R_0 = |\vec{r} - \vec{R}_t|$ and $R = |\vec{R}_r - \vec{r}|$ are distances from the point $\vec{r}$ in the plane $z = 0$ to the transmitter and to the receiver locations, respectively. The single prime and the double prime mark values related to points $\vec{r}'$ and $\vec{r}''$. Also, we assumed here that statistical averaging denoted by angular brackets is related to surface elevations only. This averaging produces $\Phi = \langle \exp[-iq_z'\zeta(\vec{r}') + iq_z''\zeta(\vec{r}'')] \rangle$, which is the double-point characteristic function of the large-scale elevation ζ.

In calculation of this function, we follow the standard procedure of the, so called, geometric optics limit applied to the case of the diffusive scattering regime characterized by the large Rayleigh parameter $q_z^2\langle \zeta^2 \rangle \gg 1$ (cf., [16], [18], [29]). Function Φ is close to unity within the area $|\vec{r}' - \vec{r}''| \le l_\Phi$, and tends to zero outside this area, where l_Φ is the characteristic scale of Φ over $\vec{r}' - \vec{r}''$. Estimations show that the diffusive regime holds for elevation angles $\theta > 20^\circ$ and seas that correspond to winds >3 m/s [16], [30]. When the Rayleigh parameter is small, $q_z^2\langle \zeta^2 \rangle < 1$ (low winds), the function Φ tends to the product, $\langle \exp[-iq_z'\zeta(\vec{r}')] \rangle \langle \exp[iq_z''\zeta(\vec{r}'')] \rangle$. This is the, so called, coherent component of the scattered power. Therefore, here we consider the case when this component can be neglected.

Now turn from $\vec{r}'$ and $\vec{r}''$ to new variables $\vec{\xi} = \vec{r}' - \vec{r}''$ and $\vec{\rho} = t(\vec{r}' + \vec{r}'')/2$. Using these variables, we expand $K(R_0' + R' - R_0'' - R'')$ into the Taylor series over $\vec{\xi}$, withholding only a linear term $-\vec{q}_\perp(\vec{\rho}) \cdot \vec{\xi}$. This limit is legitimate here because only a small area $\xi \le l_\Phi$ significantly contributes to the integral over $\vec{\xi}$ in (30). Under the same conditions one can set $\vec{\xi} = 0$ (i.e., $\vec{r}' = \vec{r}'' = \vec{\rho}$) in the pre-exponential term in (30), and $q_z' \approx q_z'' \approx q_z(\vec{\rho})$ in Φ. Upon expanding integration limits over $\vec{\xi}$ to infinity, the result can be represented as follows:

$$\begin{aligned}\langle |Y(\tau)|^2 \rangle = T_i^2 \int & \frac{D^2(\vec{\rho}) \Lambda^2[\tau - (R_0 + R)/c]}{4\pi R_0^2 R^2} \\ & \times |S[f_D(\rho) - f_c]|^2 \sigma_0(\vec{\rho}) \, d^2\rho, \end{aligned} \tag{31}$$

where the quantity

$$\sigma_0(\vec{\rho}) = \frac{|\Re(\vec{\rho})|^2}{4\pi} \frac{q^4(\vec{\rho})}{q_z^2(\vec{\rho})} \int \exp[-i\vec{q}_\perp(\vec{\rho}) \cdot \vec{\xi}] \Phi(\vec{\xi}, \vec{\rho}) \, d^2\xi \tag{32}$$

with the two-dimensional (2-D) characteristic function of elevations ζ under the integral

$$\Phi(\vec{\xi}, \vec{\rho}) = \langle \exp\{-iq_z[\zeta(\vec{\rho} + \vec{\xi}/2) - \zeta(\vec{\rho} - \vec{\xi}/2)]\} \rangle. \tag{33}$$

has the meaning of a normalized bistatic scattering cross section of the ocean surface. The width of $\sigma_0(\vec{\rho})$ over ρ determines a so-called glistening zone on the ocean surface.

There are various approaches to calculate the cross section σ_0. One of them, the geometric optics limit, is well-known for its simplicity (cf., [16], [18], [29]). It uses the fact that, as is pointed out above, only a small area $\xi \le l_\Phi$ significantly contributes to the integral over $\vec{\xi}$ in (30). Then, expanding the difference of elevations ζ in (33) into the Taylor series over ξ, and withholding a linear term, we obtain that $\Phi(\vec{\xi}, \vec{\rho}) \approx \langle \exp[-iq_z \nabla_\perp \zeta(\vec{\rho})] \rangle$. This leads to the following expression for the cross section σ_0 through the probability density function (PDF) of slopes $P(\vec{s})$

$$\sigma_0(\vec{\rho}) = \frac{\pi |\Re|^2 q^4}{q_z^4} P\left(-\frac{\vec{q}_\perp}{q_z} \right). \tag{34}$$

The cross section is maximal at $\vec{q}_\perp = 0$, because $P(\vec{s})$ has a maximum at $\vec{s} = \nabla_\perp \zeta = 0$ (i.e., for the most probable orientation of slopes, parallel to $z = 0$).

Now we can substitute (34) into (31) and obtain the final expression for the waveform

$$\begin{aligned}\langle |Y(\tau)|^2 \rangle = T_i^2 \int & \frac{|\Re|^2 D^2(\vec{\rho}) \Lambda^2[\tau - (R_0 + R)/c] q^4}{4 R_0^2(\vec{\rho}) R^2(\vec{\rho}) q_z^4} \\ & \times |S[f_D(\rho) - f_c]|^2 P\left(-\frac{\vec{q}_\perp}{q_z} \right) d^2\rho. \end{aligned} \tag{35}$$

APPENDIX B
SEA-SURFACE MODEL

In experiments with GPS signal scattering from the ocean surface [6], the down-looking antenna is designed to receive the left-hand, circular-polarized (LHCP) electromagnetic waves, because upon scattering from the ocean surface the signal acquires predominantly the opposite sign of a circular polarization; however, some small portion of the signal remains of the right-hand circular polarization (RHCP). Calculations of (35) yield 20–30 dB lower level for the RHCP signal compared to the LHCP at elevation angles $\theta > 20°$. More accurate calculations based on the Small-Slope Approximation give somewhat higher level for the RHCP signal [34]. The following equations express relationships between local Fresnel coefficients $\Re$ for different polarization modes of incident and reflected waves. Subscripts $R, L, V,$ and H stand, respectively, for right-hand circular, left-hand circular, vertical, and horizontal (with respect to the tangent plane) linear polarizations

$$\Re_{\mathrm{RR}} = \Re_{\mathrm{LL}} = \frac{1}{2}(\Re_{\mathrm{VV}} + \Re_{\mathrm{HH}}) \tag{36}$$

$$\Re_{\mathrm{RL}} = \Re_{\mathrm{LR}} = \frac{1}{2}(\Re_{\mathrm{VV}} - \Re_{\mathrm{HH}}) \tag{37}$$

where

$$\Re_{\mathrm{VV}} = \frac{\varepsilon \sin\theta - \sqrt{\varepsilon - \cos^2\theta}}{\varepsilon \sin\theta + \sqrt{\varepsilon - \cos^2\theta}} \tag{38}$$

$$\Re_{\mathrm{HH}} = \frac{\sin\theta - \sqrt{\varepsilon - \cos^2\theta}}{\sin\theta + \sqrt{\varepsilon - \cos^2\theta}} \tag{39}$$

and ε is the complex dielectric constant of sea water, and θ is the local grazing angle.

Our approach is not limited by some specific form of the slope PDF $P(\vec{s})$. In our numerical simulations, we use the Gaussian statistics of anisotropic slopes

$$P(\vec{s}) = \frac{1}{2\pi\sigma_{s_x}\sigma_{s_y}\sqrt{1-b_{x,y}^2}} \times \exp\left[-\frac{1}{2\left(1-b_{x,y}^2\right)}\left(\frac{s_x^2}{\sigma_{s_x}^2} - 2b_{x,y}\frac{s_x s_y}{\sigma_{s_x}\sigma_{s_y}} + \frac{s_y^2}{\sigma_{s_y}^2}\right)\right] \tag{40}$$

where slope variances and correlations are wind-dependent and can be derived from a sea-surface elevation spectrum $W(\vec{\kappa})$ by integration over wave numbers κ smaller than the scale dividing parameter $\kappa_* = 2\pi/3\lambda$, ($\kappa_* = 11$ rad/m for the GPS L1 carrier $\lambda = 0.19$ m)

$$\sigma_{s_{x,y}}^2 = \left\langle s_{x,y}^2 \right\rangle = \iint \kappa_{x,y}^2 W(\vec{\kappa})\, d^2\kappa \tag{41}$$

$$b_{x,y} = \langle s_x s_y \rangle / \sigma_{s_x}\sigma_{s_y} \tag{42}$$

$$\langle s_x s_y \rangle = \iint \kappa_x \kappa_y W(\vec{\kappa})\, d^2\kappa. \tag{43}$$

These general equations are valid for an arbitrary spectrum $W(\vec{\kappa})$. If the spectrum is symmetrical with respect to a wind direction, then $b_{x,y} \equiv 0$, assuming that wind is blowing along major x- or y-axes, otherwise $b_{x,y} \neq 0$. If ϕ_0 is the angle between the wind direction and y-axis, then, $\sigma_{s_x}^2$, $\sigma_{s_y}^2$, and $\langle s_x s_y \rangle$ can be readily expressed through variances $\sigma_{s_{x0}}^2$, $\sigma_{s_{y0}}^2$, defined in the $x0y0$ coordinate frame, where $y0$ coincides with the wind direction

$$\sigma_{s_x}^2 = \sigma_{s_{x0}}^2 \cos^2\phi_0 + \sigma_{s_{y0}}^2 \sin^2\phi_0 \tag{44}$$

$$\sigma_{s_y}^2 = \sigma_{s_{y0}}^2 \cos^2\phi_0 + \sigma_{s_{x0}}^2 \sin^2\phi_0 \tag{45}$$

$$\langle s_x s_y \rangle = \left(\sigma_{s_{y0}}^2 - \sigma_{s_{x0}}^2\right)\cos\phi_0 \sin\phi_0. \tag{46}$$

In our calculations, we have assumed the model for the elevation spectrum of wind-driven sea surface, presented in [31], which accounts for fetch-limited conditions. This model contains the following parameters: U_{10}, the wind speed at a height of 10 m, and inverse wave age Ω. They determine κ_p, the wave number of the dominant wave, or the spectral peak, through phase speed c_p of the dominant wave

$$c_p = \sqrt{g/k_p} = U_{10}/\Omega \tag{47}$$

For a well-developed sea, $\Omega = 0.84$.

According to [31], an elevation spectrum of wind-driven sea surface can be presented as

$$W(\vec{\kappa}) = \psi(\kappa) D(\kappa, \phi; \phi_0) \tag{48}$$

where

$$\psi(\kappa) = \kappa^{-4}[B_l(\kappa) + B_h(\kappa)] L(\kappa) \Gamma^{\gamma(\kappa)} \tag{49}$$

is the radial part of the spectrum, and

$$D(\kappa, \phi; \phi_0) = \frac{1}{2\pi}[1 + \Delta(\kappa)\cos 2(\phi - \phi_0)] \tag{50}$$

is the azimuthal part of the spectrum, where ϕ_0 is the wind direction. The term $B_l(\kappa)$ describing a correction to κ^{-4} at low frequencies is

$$B_l(\kappa) = 0.003\sqrt{\frac{\Omega\kappa}{\kappa_p}} \exp\left[-\frac{\Omega}{\sqrt{10}}\left(\sqrt{\frac{\kappa}{\kappa_p}} - 1\right)\right] \tag{51}$$

where

$$L(\kappa) = \exp\left[-\frac{5}{4}(\kappa_p/\kappa)^2\right] \tag{52}$$

$$\Gamma = \begin{cases} 1.7, & \text{for } 0.83 < \Omega < 1; \\ 1.7 + 6\log(\Omega), & \text{for } 1 < \Omega < 5. \end{cases} \tag{53}$$

The coefficient $\gamma(\kappa)$ is

$$\gamma(\kappa) = \exp\left[-\left(\kappa^{1/2} - \kappa_p^{1/2}\right)^2 \Big/ 2\delta^2\kappa_p\right] \tag{54}$$

$$\delta = 0.08(1 + 4\Omega^{-3}). \tag{55}$$

Even though our numerical algorithm includes both $B_l(\kappa)$ and $B_h(\kappa)$, we should note that the high-frequency correction term $B_h(\kappa)$ is less important for our consideration, because according to the two-scale model the variances of large-scale

slopes are determined mostly by the low-frequency region of the spectrum, $\kappa < \kappa_* = 2\pi/3\lambda$. For details on $B_h(\kappa)$ and frequency-dependent coefficient $\Delta(\kappa)$ in the azimuthal dependence (see [31]).

APPENDIX C
ANALYTICAL RESULT FOR THE CASE OF NORMAL INCIDENCE

Let us assume a low-gain (wide-beam) antenna, low altitude for the receiver $h \ll h_0$, Doppler spreading $f_c - f_D$ over the glistening surface is less than the Doppler bandwidth $\Delta f_0 = 1/T_i$ of the receiver, and elevation angle is close to 90°. The normal incidence makes polar coordinates ρ, φ more convenient for calculations. Under these conditions, we can set $\Re(\vec{\rho}) = \Re(\rho)$, $D^2 = 1$, $|S|^2 = 1$. Geometrical parameters are also simplified

$$\begin{aligned} &R_{0,\mathrm{sp}}^2 \approx R_0^2 \approx h_0^2, \quad R_{\mathrm{sp}}^2 \approx h^2, \quad R^2 \approx h^2 + \rho^2, \\ &q^2 \approx 2K^2(1 + h/\sqrt{h^2+\rho^2}), \\ &q_z \approx K(1 + h/\sqrt{h^2+\rho^2}), \quad \vec{q}_\perp \approx -K\vec{\rho}/\sqrt{h^2+\rho^2}. \end{aligned} \tag{56}$$

In the case of Gaussian isotropic PDF of slopes P, we can use (41)–(43), where we should set

$$\sigma_{s_x}^2 = \sigma_{s_y}^2 = \sigma_s^2/2, \quad b_{xy} = 0. \tag{57}$$

After introducing new, dimensionless variables $\vec{p} = \vec{\rho}/h$ and $p_0 = c\tau_0/h$, (35) becomes

$$\begin{aligned} \langle |Y(p_0)|^2 \rangle = \frac{2\pi T_i^2}{h_0^2} \int_0^\infty & \frac{\Lambda^2\left[\frac{h}{c}(p_0 + 1 - \sqrt{1+p^2})\right]}{(1+\sqrt{1+p^2})^2} \\ & \times |\Re(p)|^2 P\left(\frac{p}{1+\sqrt{1+p^2}}\right) p\, dp. \end{aligned} \tag{58}$$

Now we assume that Λ^2-function is narrower than all others in the integrand, i.e., it can be approximately expressed as

$$\Lambda^2\left[\frac{h}{c}(p_0 + 1 - \sqrt{1+p^2})\right] \approx \Sigma_0 \delta[p^2 - p_0(p_0+2)]. \tag{59}$$

The normalization factor Σ_0 in front of the delta function in (59) can be obtained by integrating both parts of this equation multiplied by p

$$\begin{aligned} &\int_0^\infty \Lambda^2\left[\frac{h}{c}(p_0 + 1 - \sqrt{1+p^2})\right] p\, dp \\ &\quad \approx \Sigma_0 \int_0^\infty \delta[p^2 - p_0(p_0+2)] p\, dp = \frac{\Sigma_0}{2}. \end{aligned} \tag{60}$$

Upon substituting (20) into (60) and performing the integration, we obtain the following expression for Σ_0 at $p_0 \geq p_* = c\tau_c/h$:

$$\Sigma_0 = \frac{4p_*}{3}(1 + p_0). \tag{61}$$

Thus, an analytical expression for the waveform at normalized delays $p_0 \geq p_*$ is

$$\langle |Y(p_0)|^2 \rangle = \frac{T_i^2 A(p_0)}{h_0^2 \sigma_s^2} \exp\left\{-\frac{b(p_0)}{\sigma_s^2}\right\} \tag{62}$$

where

$$A(p_0) = \frac{4p_*(1+p_0)|\Re[\theta = 1/\sqrt{p_0(2+p_0)}]|^2}{3[1+\sqrt{1+p_0(2+p_0)}]^2} \tag{63}$$

$$b(p_0) = \frac{p_0(2+p_0)}{[1+\sqrt{1+p_0(2+p_0)}]^2}. \tag{64}$$

Note that the power reflection coefficient $|\Re|^2$ can be calculated using (36)–(39).

ACKNOWLEDGMENT

The authors wish to thank E. Walsh of the NASA Goddard Space Flight Center, Greenbelt, MD, for stimulating their interest in this problem. The authors would like to thank S. Katzberg of the NASA Langley Research Center, J. Garrison of the NASA Goddard Space Flight Center, and G. Born, P. Axelrad, and A. Komjathy of the University of Colorado, Boulder, for fruitful discussions. Finally, they are grateful to the anonymous reviewer for helpful suggestions.

REFERENCES

[1] M. Martin-Neira, "A passive reflectometry and interferometry system (PARIS): Application to ocean altimetry," *ESA J.*, vol. 17, pp. 331–355, 1993.

[2] K. D. Anderson, "A GPS tide gauge," *GPS World Showcase*, vol. 6, pp. 44–44, Aug. 1995.

[3] J.-C. Auber, A. Bibaut, and J.-M. Rigal, "Characterization of multipath on land and sea at GPS frequencies," in *ION GPS-94*, Salt Lake City, UT, Sept. 20, 1994, pp. 1155–1171.

[4] S. J. Katzberg and J. L. Garrison Jr., "Utilizing GPS to Determine Ionospheric Delay over the Ocean,", NASA Tech. Memo 4750, Dec. 1996.

[5] J. L. Garrison, S. J. Katzberg, and C. T. Howell III, "Detection of ocean reflected GPS signals: Theory and experiment," in *Proc. IEEE Southeastcon'97: Engineering the New Century*. Blacksburg, VA, 1997, pp. 290–294.

[6] J. L. Garrison, S. J. Katzberg, and M. I. Hill, "Effect of sea roughness on bistatically scattered range coded signals from the global positioning system," *Geophys. Res. Lett.*, vol. 25, pp. 2257–2260, 1998.

[7] S. F. Clifford, V. I. Tatarskii, A. G. Voronovich, and V. U. Zavorotny, "GPS sounding of ocean surface waves: Theoretical assessment," in *Proc. IEEE Int. Geoscience and Remote Sensing Symp.: Sensing and Managing the Environment, 98CH36174*. Piscataway, NJ, 1998, pp. 2005–2007.

[8] A. Komjathy, V. Zavorotny, P. Axelrad, G. Born, and J. Garrison, "GPS signal scattering from sea surface: Comparison between experimental data and theoretical model," in *Proc. 5th Int. Conf. Remote Sensing for Marine and Coastal Environments*, vol. 1, San Diego, CA, Oct. 5–7, 1998, pp. 530–539.

[9] A. Komjathy, J. L. Garrison, and V. Zavorotny, "GPS: A new tool for ocean science," *GPS World*, vol. 10, pp. 50–56, Apr. 1999.

[10] D. E. Wells, N. Beck, D. Delikaraoglou, A. Kleusberg, E. J. Krakiwsky, G. Lachapelle, R. B. Langley, M. Nakiboglu, K. P. Schwarz, J. M. Tranquilla, and P. Vaníček, *Guide to GPS Positioning*. Fredericton, N.B., Canada: Canadian GPS Assoc., 1987.

[11] B. Hofmann-Wellenhof, H. Lichtenegger, and J. Collins, *Global Positioning System. Theory and Practice*, 3rd ed. New York: Springer-Verlag, 1994.

[12] B. W. Parkinson, J. J. Spilker, P. Axelrad, and P. Enge, Eds., *Global Positioning System Theory and Applications*. Washington, DC: Amer. Inst. Astron. Aero., 1996, vol. 163.

[13] S. W. Golomb, Ed., *Digital Communications with Space Applications*. Englewood Cliffs, NJ: Prentice-Hall, 1964.
[14] F. E. Nathanson, *Radar Design Principles*. New York: McGraw-Hill, 1969.
[15] G. R. Valenzuela, "Theories for the interaction of electromagnetic and oceanic waves—A review," *Bound.-Layer Meteorol.*, vol. 31, pp. 61–85, 1978.
[16] F. G. Bass and I. M. Fuks, *Wave Scattering from Statistically Rough Surfaces*, C. B. Vesecky and J. F. Vesecky, Eds. Oxford, U.K.: Pergamon, 1979, vol. 93.
[17] P. Beckmann and A. Spizzichino, *The Scattering of Electromagnetic Waves from Rough Surfaces*. New York: Pergamon, 1963.
[18] S. M. Rytov, Yu. A. Kravtsov, and V. I. Tatarskii, *Principles of Statistical Radiophysics, vol. 4: Wave Propagation through Random Media*, Berlin, Germany: Springer-Verlag, 1988.
[19] A. G. Voronovich, *Wave Scattering from Rough Surfaces*, Berlin, Germany: Springer-Verlag, 1994.
[20] D. L. Hammond, R. A. Mennella, and E. J. Walsh, "Short pulse radar used to measure sea surface wind speed and SWH," *IEEE J. Oceanic Eng.*, vol. OE-2, pp. 61–67, 1977.
[21] G. S. Brown, "Backscattering from a Gaussian-distributed, perfectly conducting rough surface," *IEEE Trans. Antennas Propagat.*, vol. AP-26, pp. 472–482, 1978.
[22] F. C. Jackson, W. T. Walton, D. E. Hines, B. A. Walters, and C. Y. Peng, "Sea surface mean square slope from K_u-band backscatter data," *J. Geophys. Res.*, vol. 97, pp. 11 411–11 427, 1992.
[23] B. L. Lewis, F. F. Kretschmer Jr., and W. W. Shelton, *Aspects of Radar Signal Processing*. Boston, MA: Artech House, 1986.
[24] D. K. Barton, *Modern Radar System Analysis*. Boston, MA: Artech House, 1988.
[25] A. W. Rihaczek, *Principles of High Resolution Radar*. New York: McGraw-Hill, 1969.
[26] J. K. Holmes, *Coherent Spread Spectrum Systems*. New York: Wiley, 1982.
[27] G. Jourdain and J. P. Henrioux, "Use of large bandwidth-duration binary phase shift keying signals in target delay Doppler measurements," *J. Acoust. Soc. Amer.*, vol. 90, pp. 299–309, 1991.
[28] C. Elachi, *Spaceborne Radar Remote Sensing: Applications and Techniques*. New York: IEEE Press, 1988.
[29] D. E. Barrick, "Relationship between slope probability density function and the physical optics integral in rough surface scattering," *Proc. IEEE*, vol. 56, pp. 1728–1729, 1968.
[30] A. G. Voronovich, "On the theory of electromagnetic waves scattering from the sea surface at low grazing angles," *Radio Sci.*, vol. 31, pp. 1519–1530, 1996.
[31] T. Elfouhaily, B. Chapron, K. Katsaros, and D. Vandemark, "A unified directional spectrum for long and short wind-driven waves," *J. Geophys. Res.*, vol. 102, pp. 15 781–15 796, 1997.
[32] A. G. Voronovich, "Small slope approximation for electromagnetic wave scattering at a rough interface of two dielectric half-spaces," *Waves in Random Media*, vol. 4, pp. 337–367, 1994.
[33] V. I. Tatarskii, "Formulation of rough-surface scattering theory in terms of phase factors and approximate solutions based on this formulation," *Waves in Random Media*, vol. 7, pp. 557–578, 1997.
[34] V. U. Zavorotny and A. G. Voronovich, "Bistatic radar scattering from an ocean surface in the small-slope approximation," in *Proc. IEEE Int. Geoscience and Remote Sensing Symp.: Remote Sensing of the System Earth—A Challenge for the 21st Century, 99CH36293*. Piscataway, NJ, 1999, pp. 2419–2421.

Valery U. Zavorotny received the degree in radio physics from Gorky State University, Gorky, Russia, in 1971, and the Ph.D. degree in physics and mathematics from the Institute of Atmospheric Physics of USSR Academy of Sciences, Moscow, Russia, in 1979.

From 1971 to 1990, he was a Research Scientist with the Institute of Atmospheric Physics of USSR Academy of Sciences. In 1990, he joined Lebedev Physical Institute, Moscow. Since 1991, he has been a Research Scientist with the Cooperative Institute for Research in Environmental Sciences and the Environmental Technology Laboratory, University of Colorado, National Oceanic and Atmospheric Administration (NOAA), Boulder, CO. His research interests include wave scattering from rough surfaces, optical and radio wave propagation through random media, ocean and atmospheric remote sensing techniques.

Alexander G. Voronovich received the degree in physics and the Ph.D. degree in theoretical and mathematical physics from Moscow Institute of Physics and Technology, Moscow, Russia, in 1972 and 1975, respectively, and the Dr.Sci ence degree in theoretical and mathematical physics from the Acoustical Institute, Moscow, in 1988.

From 1975 to 1979, he was a Junior Research Scientist with the Acoustical Institute, Moscow. In 1980, he joined P. P. Shirshov Institute of Oceanology, Moscow, as a Senior Research Scientist, and became a Professor of Physics at the Moscow Institute of Physics and Technology in 1991. From 1989 to 1993, he was a Head of the Laboratory of Acoustical Waves Propagation in the Ocean, P. P. Shirshov Institute of Oceanology. He is currently an Oceanographer at the Environmental Technology Laboratory, National Oceanic and Atmospheric Administration (NOAA), Boulder, CO. His research interests include wave scattering from rough surfaces, ocean acoustics, geophysical hydrodynamics, internal waves, and linear and nonlinear theory of wave propagation.

Dr. Voronovich is a Fellow of the Acoustical Society of America.